

Nonmonotonic band gap evolution in bent phosphorene nanosheets

Vojtěch Vlček,^{1,*} Eran Rabani,^{2,3,†} Roi Baer,^{4,‡} and Daniel Neuhauser^{5,§}

¹*Department of Chemistry and Biochemistry, University of California, Santa Barbara, California 93106, USA*

²*Department of Chemistry, University of California and Materials Science Division, Lawrence Berkeley National Laboratory, Berkeley, California 94720, USA*

³*The Raymond and Beverly Sackler Center for Computational Molecular and Materials Science, Tel Aviv University, Tel Aviv 69978, Israel*

⁴*Fritz Haber Center for Molecular Dynamics, Institute of Chemistry, The Hebrew University of Jerusalem, Jerusalem 91904, Israel*

⁵*Department of Chemistry and Biochemistry, University of California, Los Angeles, California 90095, USA*



(Received 18 January 2019; revised manuscript received 18 April 2019; published 7 June 2019)

Nonmonotonic bending-induced changes of fundamental band gaps and quasiparticle energies are observed for realistic nanoscale phosphorene nanosheets. Calculations using stochastic many-body perturbation theory show that even slight curvature causes significant changes in the electronic properties. For small bending radii (<4 nm) the band gap changes from direct to indirect. The response of phosphorene to deformation is strongly anisotropic (different for zigzag vs armchair bending) due to an interplay of exchange and correlation effects. Overall, our results show that fundamental band gaps of phosphorene sheets can be manipulated by as much as 0.7 eV depending on the bending direction.

DOI: [10.1103/PhysRevMaterials.3.064601](https://doi.org/10.1103/PhysRevMaterials.3.064601)

I. INTRODUCTION

Since its discovery less than a decade ago [1–3], single layer phosphorene attracted much attention due to its unique electronic and mechanical properties. Its fundamental band gap (E_g) can be tuned by increasing the number of stacked monolayers [4–6] or by chemical doping [7], and spans a wide range of values, from $E_g = 1.88$ eV in single layer phosphorene to $E_g = 0.3$ eV in the bulk. The unique mechanical properties [8] along with high room temperature mobilities (around 1000 cm²/sV) [3] make phosphorene a promising candidate for fabrication of next generation flexible nanoelectronics [3,9–12] nanophotonics [13], and ultrasensitive sensors [14,15].

Understanding the interplay between the electronic and mechanical properties is central for future technological developments. Indeed, significant progress has been made in describing the role of strain. Density functional theory (DFT) calculations predict a decrease in the band gap as a result of the application of uniaxial strain, which ultimately results in a direct-to-indirect band gap transition [16,17]. However, DFT is not a good proxy for quasiparticle energies [18,19]. The case of bent phosphorene is even more challenging, since investigation of bending effects naturally precludes the use of periodic boundary conditions. In practice, bending along a single direction requires simulations of large finite systems. Thus so far only small systems were simulated, for example, narrow [quasi-one-dimensional (1D)] phosphorene nanoribbons [20] studied with DFT, indicating charge

localization and formation of in-gap states for extreme bending conditions (radii $R < 1.3$ nm). These bending scenarios are very challenging experimentally.

Ab initio many-body perturbation theory in the *GW* approximation [21–23] yields accurate predictions for quasiparticle energies. Its cost was prohibitive, however, so *GW* was only feasible for small and medium sized systems [24,25]. Luckily, the costs are drastically reduced by a new stochastic approach to simulating *GW*, labeled Stochastic*GW* or just *sGW* [26–29], which is a part of a general stochastic paradigm [30–35]. *sGW* is sufficiently efficient that it is less expensive than the underlying DFT stage, and this makes it possible to treat systems with thousands of electrons or more [27,29]. We employ here *sGW* for calculating quasiparticle (QP) energies for simply bent phosphorene; since a periodic boundary condition cannot be applied, we consider a series of large phosphorene nanosheets (PNS) with dimensions of 2.9×4.3 nm.

The PNS are subject to bending with radii between $1 \mu\text{m}$ and 2 nm—a range that can be realized experimentally [36,37]. Thus it is possible to directly map the evolution of band gaps with deformation of a 2D material. We discover here that even a small sample curvature affects the QP energies and that DFT severely underestimates the response to bending. Further, irrespective of the direction of bending, we find an interesting crossing of the lowest unoccupied states leading to a change of character of the gap for radii <4 nm. The PNS response is strongly anisotropic and is governed by nontrivial interplay of exchange and correlation effects. Our results predict that, under realistic conditions, the QP gap can be manipulated solely by deformation by as much as 0.7 eV.

II. THEORY AND METHODS

Fundamental band gaps are defined as differences between ionization potential and electron affinity, which correspond to

*vlcek@ucsb.edu

†eran.rabani@berkeley.edu

‡roi.baer@huji.ac.il

§dxn@ucla.edu

quasiparticle (QP) energies of the highest occupied ($\varepsilon_H^{\text{QP}}$) and lowest unoccupied states ($\varepsilon_L^{\text{QP}}$), i.e.,

$$E_g = \varepsilon_L^{\text{QP}} - \varepsilon_H^{\text{QP}}. \quad (1)$$

While density functional theory yields a set of eigenstates and corresponding eigenvalues, those cannot be interpreted as QP energies [18]. Indeed, DFT eigenvalue differences severely underestimate true band gaps [19]. A solution is to calculate ε^{QP} through many-body perturbation theory with Kohn-Sham (KS) DFT as a starting point [22,23,38].

KS eigenvalues (ε^{KS}) contain contributions from kinetic energy and Hartree, ionic, and a mean field exchange-correlation (xc) potential energies. The QP energy is obtained by replacing the xc term (v_{xc}) by exchange (Σ_X) and polarization self-energies (Σ_P):

$$\varepsilon^{\text{QP}} = \varepsilon^{\text{KS}} - v_{xc} + \Sigma_X + \Sigma_P(\varepsilon^{\text{QP}}). \quad (2)$$

The exchange contribution is

$$\Sigma_X = - \sum_j^{N_{\text{occ}}} \iint \phi(\mathbf{r})\phi_j(\mathbf{r}) \frac{1}{|\mathbf{r} - \mathbf{r}'|} \phi_j(\mathbf{r}')\phi(\mathbf{r}') d\mathbf{r} d\mathbf{r}', \quad (3)$$

where ϕ is the orbital for which ε^{QP} is evaluated and the sum extends over all N_{occ} occupied states. Σ_P is a dynamical quantity describing the polarization of the density due the QP. Note that Eq. (2) is a fixed point equation, where Σ_P is evaluated at the frequency corresponding to ε^{QP} .

The self-energy terms are computed using *sGW*, which, as mentioned, scales nearly linearly with the number of electrons and allows one to compute Σ for extremely large systems with thousands of atoms [29]. While the *GW* approximation should in theory be solved by a self-consistent set of Hedin's equations [21], it is common practice to use a one-shot correction (G_0W_0), in which the self-energy is based on the underlying KS Hamiltonian. This is, however, insufficient in many cases [19]. We thus rely on a partially self-consistent $\bar{\Delta}GW_0$ approach [39] which is a simple postprocessing step on top of G_0W_0 and yields band gaps in excellent agreement with experiment [39].

III. RESULTS

We investigated the effects of bending on a set of phosphorene nanosheets derived from the experimental structure of bulk black phosphorus [40]. PNS were constructed from a 10×10 single sheet supercell passivated with hydrogen atoms. We relaxed the interatomic positions using a reactive force field developed for low dimensional phosphorene systems [41]. First principles geometry minimization, e.g., with DFT, is too expensive due to the size of the system. The relaxation was performed such that the phosphorus atoms that are on the straight edge were fixed and the structure optimized within the LAMMPS code [42,43].

A ground state DFT calculation was performed using a real-space grid representation, ensuring (through the Martyna-Tuckerman approach [44]) that the potentials are not periodic. The exchange-correlation interaction was described by the local density approximation (LDA) [45] with Troullier-Martins pseudopotentials [46]. With a kinetic energy cutoff

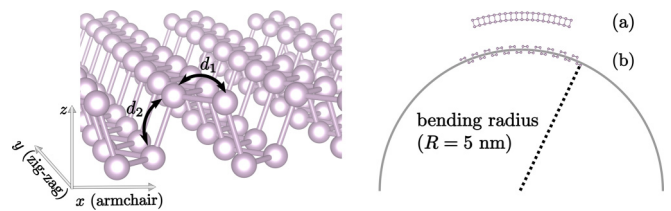


FIG. 1. Phosphorene is characterized by puckered honeycomb lattice with ridges along the armchair (x) axis. Two nearest neighbor distances are denoted in the left panel (d_1 and d_2). Bending of PNS is illustrated on the right for bending radius $R = 5$ nm; PNS bent along zigzag and armchair axes are on the top denoted as (a) and (b), respectively. Note that a plane separating the “inner” and “outer” phosphorus atoms is on the surface of a cylinder with radius R .

of $26E_h$ and $0.6a_0$ real-space grids spacing the Kohn-Sham eigenvalues were converged to <10 meV.

Many-body calculations were performed using the StochasticGW code [47] with 40 000 fragmented stochastic bases. Only quasiparticle energies were computed, while we kept the DFT orbitals unchanged. The dynamical part of the self-energy was computed using eight stochastic orbitals in each stochastic sampling of Σ_P using the random-phase approximation (i.e., time-dependent Hartree) and with a propagation time of 100 atomic units. The total number of stochastic samples was varied to reach a statistical error of ≤ 0.02 eV for the QP energies (typically 1200 samples).

A. Planar phosphorene nanosheet

Ideal phosphorene has a puckered honeycomb structure with two distinct in-plane directions: armchair (x) and zigzag (y) as shown in Fig. 1. The characteristic ridges in the structure are along the zigzag direction. Each phosphorus atom has two nearest neighbor distances d_1 and d_2 constituting a ridge. In two extreme scenarios, the bending axis is either along the x (armchair) or y (zigzag) directions (Fig. 1), resulting in nonuniform interatomic distances.

To focus our investigation purely on the effect of PNS bending, we first construct an ideal phosphorene monolayer with dimensions 4.3×2.9 nm along the armchair and zigzag directions with 1,958 valence electrons. The arrangement of the P atoms is identical to a layer of the periodic P crystal [40] and thus our results can be compared to previous calculations for infinite 2D systems.

We find that for a planar PNS, one-shot G_0W_0 predicts a quasiparticle band gap of $E_g = 2.23 \pm 0.04$ eV. This is larger by ~ 0.2 eV than E_g for bulk systems [4,5,48]. Self-consistency ($\bar{\Delta}GW_0$) further increases the fundamental band gap to $E_g = 2.47 \pm 0.04$ eV. Our $\bar{\Delta}GW_0$ result overlaps a previous study of infinite 2D sheets of phosphorene at the G_1W_1 level (obtained in first iteration to self-consistency) [4] but is larger by 0.17 eV than a similar self-consistent treatment (GW_0) for bulk [49]. The larger fundamental gap indicates that the large PNS considered here is still slightly influenced by quantum confinement, but to a much smaller degree than several small systems that were previously studied by DFT [20,50]. This shows the strength of *sGW*, which provides reliable results for quasiparticle energies of extended systems.

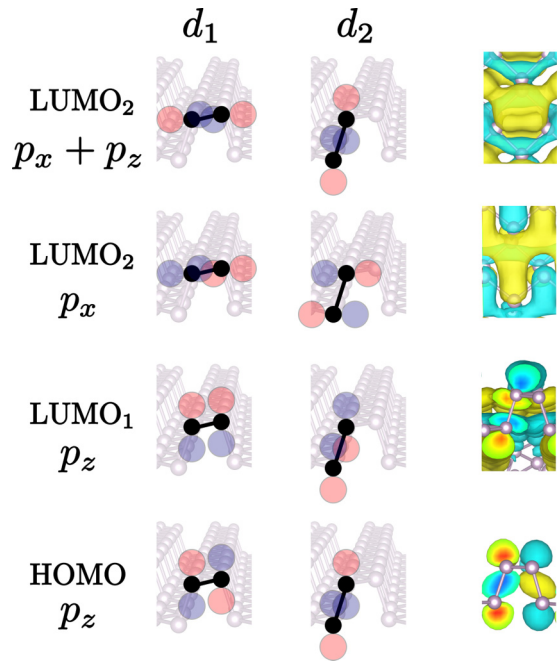


FIG. 2. Orbital character for the band-edge states. Simplified overlaps of two nearest neighbors with interatomic distances d_1 and d_2 are depicted separately for clarity. Identical colors in the p -orbital lobes correspond to a bonding overlap; distinct colors depict an antibonding overlap. The rightmost column shows details of the orbital isosurfaces. The character of the HOMO state does not change with bending. LUMO₁ is the lowest unoccupied state for radii $R \geq 4$ nm. LUMO₂ (see text for reference) has either an antibonding p_x character (for $R < 4$ nm in zigzag bending) or mixed $p_x + p_z$ character (for $R < 4$ nm in armchair bending).

By inspecting the nature of individual states (Fig. 2), we find that the valence band maxima and the conduction band minima have a p_z orbital character. In a simplified picture, the p orbitals are centered on each P atom and their hybridization forms bonding and antibonding states. This is qualitatively shown in the HOMO and LUMO in Fig. 2. Since bending (discussed later) changes the orbital ordering, we denote the lowest unoccupied state in a planar system as LUMO₁, for clarity.

Both HOMO and LUMO₁ states are strongly delocalized around the center of the PNS and extend to the edges along the armchair (x) direction (see the left isosurfaces in Figs. 3 and 4, in the limit $R \rightarrow \infty$). The delocalization along the armchair direction is associated with an effective mass that is seven times lower along the armchair direction compared to the zigzag direction [17]. The orientation and phase of the orbitals do not change markedly when translating by a unit-cell vector along x or y direction. This indicates that both HOMO and LUMO₁ are in phase, consistent with previous calculations for bulk [16,17,50], supporting a direct band-gap material.

The calculations above were done for ideal sheet geometries. We also studied phosphorene nanosheets with a reactive force field which was tuned to reproduce the elastic properties of phosphorene [41]. Relaxation affects mainly atoms at the edge and shortens the d_2 distance by 0.03 Å. As a result, the d_1 and d_2 bond lengths are almost identical, leading to

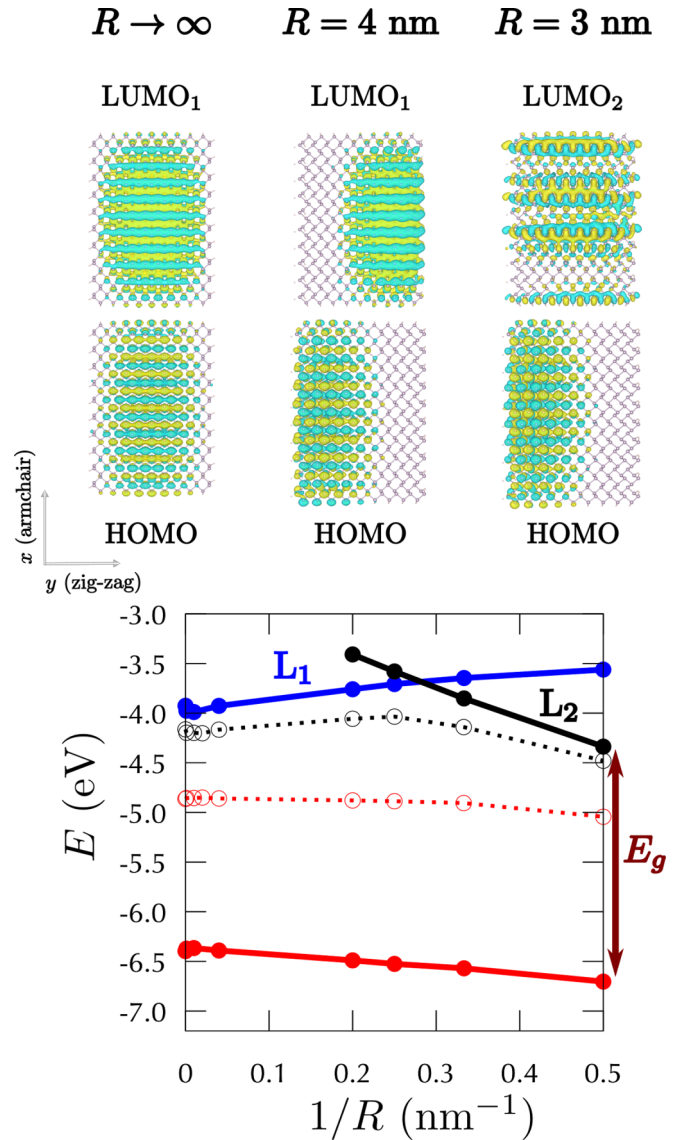


FIG. 3. Top: orbital isosurfaces for bending along the zigzag axis; the phase of the wave function is distinguished by its color. Bottom: QP energies in zigzag bending obtained by LDA (squares) and ΔGW_0 (circles). The stochastic error of ΔGW_0 for each point is smaller than the symbol size. The HOMO state is shown in red, LUMO₁ (denoted L_1) in blue, and LUMO₂ (denoted L_2) in black. For simplicity, we do not distinguish LUMO₁ and LUMO₂ in the DFT results, which always refer to the lowest unoccupied state. The fundamental band gap E_g is shown for $R = 2$ nm and the specific values are reproduced in Table I. Note that LUMO₂ is identified for $R = 5$ as the fifth state above LUMO₁ (for clarity we do not depict intermediate states). The solid lines are linear fits of the changes of the QP energies in Table III; the dotted lines show the exchange contribution to the changes of the QP energies. These are described by Eq. (4) and the coefficients given in Table II.

stabilization of the p_x character at the expense of p_z states [5,6,16,17], signifying that the particular ordering of electronic states in phosphorene is very sensitive to the geometry. In the next subsection, we illustrate however that while the quasiparticle band gaps change dramatically and qualitatively

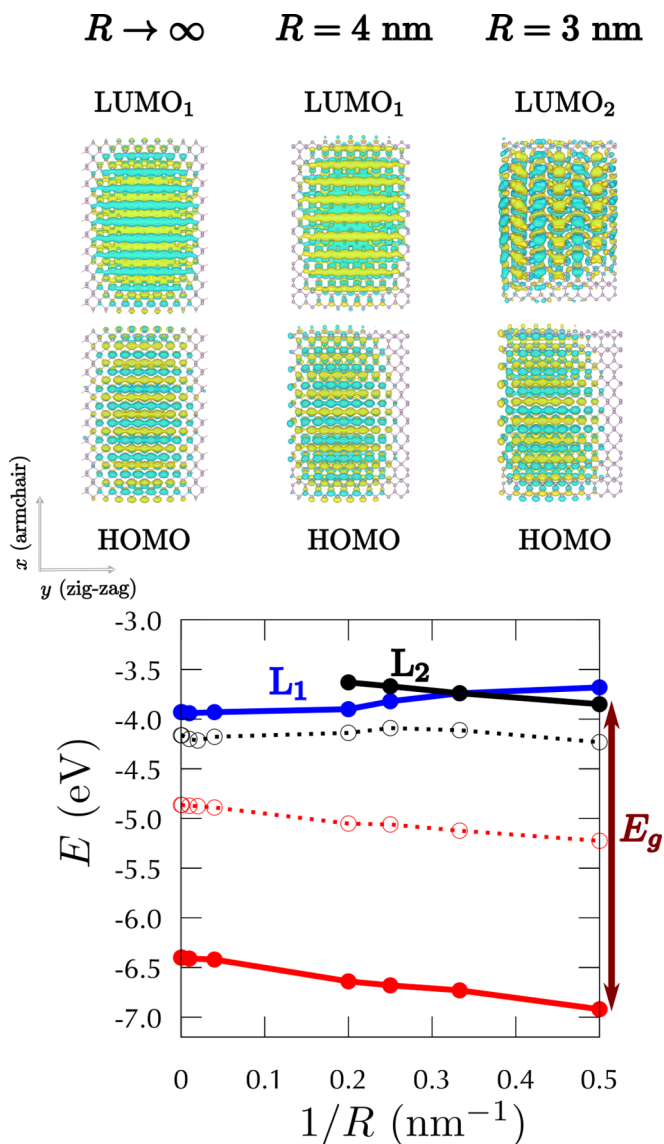


FIG. 4. Top: orbital isosurfaces for bending along the armchair axis. Bottom: QP energies for PNS bent along the armchair direction obtained by LDA (squares) and $\bar{\Delta}GW_0$ (circles). We only show the lowest energy LUMO in the DFT results.

by bending, these gaps do not depend on the precise geometry of the monolayer.

B. Bent phosphorene nanosheet

Most of the bending studies below were done with ideally bent sheets; specifically the sheet was bent by placing it on a surface of a cylinder with radius R as illustrated in Fig. 1. The plane separating the “inner” and “outer” phosphorus atoms (along the z axis) is positioned on a surface of the cylinder. In the latter part of this section we discuss bent sheets that are relaxed by force fields, where again the effects of the force-field relaxation are not large.

1. Zigzag bending

Even the slightest deformation along the zigzag direction (the y axis of the sheet is bent; see Fig. 1) results in changes

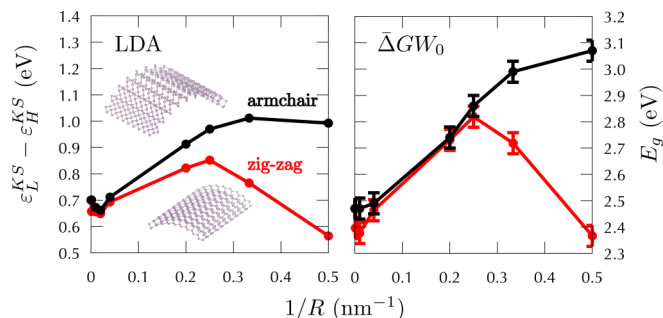


FIG. 5. Eigenvalue and fundamental band gaps (E_g) of phosphorene sheets bent along the armchair (black) and zigzag (red) directions. Bent structures for $R = 2$ nm are illustrated in the insets: top for armchair bending and bottom for zigzag. Error bars show the stochastic errors. The lines are guides for the eye.

in quasiparticle energies (Fig. 3). For large bending radii between $1 \mu\text{m}$ and 100 nm (see inset in the bottom panel of Fig. 3) the HOMO energy increases and the LUMO₁ energy decreases with bending radius. The fundamental band gap consequently drops by 0.10 ± 0.04 eV; this is clearly seen in Fig. 5 which shows the evolution of E_g with $1/R$. In DFT, a qualitatively similar effect is observed though its magnitude is $\sim 50\%$ smaller. Note that for such large R the change in the atomic positions is rather small, $<0.2\%$. This drop in E_g is accompanied by left-right symmetry breaking (along the y axis) that allows the HOMO and LUMO₁ orbitals to shift towards the edges, as discussed in the next section.

If the bending radius is further decreased ($100 \text{ nm} > R > 4 \text{ nm}$), the HOMO and LUMO₁ states gradually shift even more towards opposite edges parallel to the bending axis but remain extended along the armchair direction (Fig. 3). The energies of both states depend nearly linearly on the inverse bending radius as shown in the bottom panel of Fig. 3. The HOMO QP energy decreases with a slope of -0.71 eV nm, but LUMO₁ increases with a slope of 1.05 eV nm. As a result, the fundamental band gap opens up with decreasing bending radius. For $R = 4$ nm the band gap rises to 2.82 ± 0.02 eV, significantly larger than the band gap for planar PNS (2.47 ± 0.04 eV), as shown in Fig. 5.

DFT gaps also depend on the bending radius, but to a smaller degree. For HOMO and LUMO₁ the slopes are only -0.14 eV nm and 0.65 eV nm. The first number is five times smaller than the associated $\bar{\Delta}GW_0$ slope. Together, for intermediate R the DFT eigenvalue gap changes three times less than in $\bar{\Delta}GW_0$.

For very small bending radii (<4 nm), we observe a transition in the order of LUMO₁ and LUMO₂. The latter is nearly triply degenerate and becomes the lowest unoccupied orbital. As a result, the band gap decreases with bending radius and for $R = 2$ nm the band gap is $E_g = 2.37 \pm 0.04$ eV, i.e., even lower than the bulk value (cf. Fig. 5). By $R = 2$ nm, for both DFT and $\bar{\Delta}GW_0$, the zigzag-bending gap closes back to its planar value, due to the state crossing of the LUMOs (see Fig. 3), although the overall change of the DFT eigenvalues as R is decreased is smaller than that of the many-body calculation (see Fig. 5).

At any bending radius, both HOMO and LUMO₁ retain their p_z character. Similarly, LUMO₂, which is triply degenerate, has a p_x character (and, as mentioned, dips below LUMO₁ when the bending radius is smaller than 4 nm).

LUMO₂ is characteristically delocalized over the ridges (i.e., along the zigzag direction). Some examples of orbital isosurfaces (including one of the three LUMO₂ states) are shown in Fig. 3. Specifically, for the outer (dilated) surface of the phosphorene nanosheet, the neighboring P atoms exhibit antibonding p_x overlap. In contrast, for atoms on the inner (contracted) surface the overlap has a bonding character. LUMO₂ is localized on every other ridge along the armchair direction, i.e., it has periodicity twice as long as that of HOMO. This indicates that the fundamental band gap becomes indirect. The preceding discussion and the plot in Fig. 3 were for one of the LUMO₂ states, but the two other LUMO₂ states behave similarly.

2. Armchair bending

The PNS is also sensitive to bending along the armchair direction, as summarized in Fig. 4, but the overall trends are quite different. Now, both HOMO and LUMO₁ shift negligibly towards the armchair edges. Unlike zigzag bending, E_g remains practically constant till R is lower than 100 nm and increases when the system is further bent. This is quantitatively shown in Fig. 5. The underlying DFT gap again slightly decreases (by 0.04 eV).

The increase in the fundamental gap for $R < 100$ nm is mainly due to a shift of the HOMO QP energy that decreases linearly with a slope of -1.05 eV nm. In contrast, the slope of the LDA HOMO eigenvalue is lower by $\sim 30\%$. For radii < 4 nm, we also observe a crossing of the two unoccupied states, as was the case for zigzag bending. The shape of LUMO₂ in this armchair bending case is, however, quite different. LUMO₂ has now a mixed p_z and p_x character and its phase is roughly four times larger than a single unit cell, while HOMO and LUMO₁ have the same spatial periodicity as the ionic structure. This suggests that, for highly bent systems, the band gap is indirect. We further observe that the LUMO₂ decreases slowly: $\bar{\Delta}GW_0$ yields a slope of -0.66 eV nm, which is very similar to the LDA slope of -0.71 eV nm.

For small R , E_g opens with a mild positive slope of 0.39 eV nm, mainly due to the steep decrease of the HOMO QP energy. In contrast, the DFT eigenvalue gap remains practically constant because both the HOMO and LUMO eigenvalues shift nearly identically with $1/R$.

Note that, for $R = 2$ nm, $\bar{\Delta}GW_0$ yields $E_g = 3.08 \pm 0.02$ eV, which is 0.7 eV larger than for similar zigzag bending and 0.6 eV larger than for a planar phosphorene. For DFT, the armchair-zigzag difference at $R = 2$ nm is smaller, 0.43 eV. The QP band gaps are shown in Fig. 5 and, for selected radii, in Table I.

3. Force-field-optimized bent structures

We have also computed band gaps for relaxed phosphorene nanosheets with $R = 4$ and 2 nm. The geometries were relaxed, keeping fixed the positions of the edge P atoms. As mentioned earlier, with force-fields relaxation even for a planar ($R \rightarrow \infty$) structure the lowest LUMO has a p_x

TABLE I. Fundamental band gaps for ideally planar ($R \rightarrow \infty$) PNS and two bent systems with radii $R = 4$ and 2 nm along the zigzag and armchair axes. The stochastic error is 0.04 eV in all cases.

	$R \rightarrow \infty$		$R = 4$ nm		$R = 2$ nm	
	LDA	$\bar{\Delta}GW_0$	LDA	$\bar{\Delta}GW_0$	LDA	$\bar{\Delta}GW_0$
Zigzag	0.70	2.47	0.85	2.82	0.56	2.37
Armchair	0.70	2.47	0.97	2.84	0.99	3.07

character, and bending along the zigzag direction does not lead to state crossing. The LUMO keeps a p_x character, and its energy decreases with bending radius.

In contrast, when a force-field relaxed structure is bent along the armchair direction, the p_z -type orbital becomes a tiny bit more stable than the p_x one. The difference is so small that both LUMO states are practically degenerate.

In spite of the difference in state character between the idealized and force-field optimized structures, they both show the same difference (0.7 eV) between the QP band gaps of zigzag and armchair bent structure at $R = 2$ nm. Therefore, the precise state ordering depends on geometrical details, but the overall response to bending is highly anisotropic.

IV. DISCUSSION

A. Small curvatures

We now turn to analyze the results, and start with large R . Here, the behavior described in the previous section is remarkable. Recall that upon a tiny change of curvature in the zigzag direction (from $R \rightarrow \infty$ to $R \geq 100$ nm), the band gap decreases by about 0.1 eV (Fig. 5). This is not a big change compared with the changes at $R \sim 2-4$ nm, but it occurs with only a tiny modification of geometry.

To understand this zigzag induced 0.1 eV change, we need to first recall that the system is highly anisotropic. Figure 3 shows that HOMO and LUMO₁ are strongly confined only along the armchair direction. This is consistent with the highly anisotropic effective masses of electrons and holes (0.16/0.15 m_e and 1.24/4.92 m_e along the armchair and zigzag directions, respectively, for electrons/holes [17]). Even for tiny bending (i.e., at any finite R), the HOMO and LUMO₁ can easily migrate to the sides along the zigzag direction, as shown in Fig. 3. The energy required to localize the orbitals along the y axis is negligible due to the large effective mass along the zigzag direction.

The DFT gap also decreases initially, but by a small amount, which is independent of bending direction (unlike $\bar{\Delta}GW_0$ where the initial decrease is direction dependent, although the decrease is quite small so that it could be meddled due to statistical error effects). Note that the initial DFT decrease (at small curvatures) happens for quite a small strain—for $R = 100$ nm the strain is at most 0.02%. This suggests even a small curvature of real finite samples can somewhat change the fundamental gaps. The system size is important here, since previous calculations on periodic systems [17] required a large amount of strain (higher than 1%) to achieve a similar band gap modification.

TABLE II. Parameters O_1 and O_2 extracted from a fit of $\Delta\Sigma_X$ to changes of the interatomic distances [Eq. (4)]; errors of the fit are estimated from the standard deviations of Σ_X from the linear fit.

	O_1 (eV nm)	O_2 (eV nm)
HOMO	3.22 ± 0.03	-4.63 ± 0.01
LUMO ₁	-4.22 ± 0.01	5.03 ± 0.01
LUMO ₂ (p_x)	2.94 ± 0.01	

Big changes in the gap only occur (in both DFT and $\bar{\Delta}GW_0$) for large curvatures, discussed next.

B. Large curvatures

We now turn to large-curvature bending, with R between 100 nm and 2 nm.

The QP gaps for selected radii are shown in Table I. The variation of E_g stems from two contributions: exchange (Σ_X) and polarization (Σ_P). The latter term contains all electronic correlation including the electrodynamic (Coulomb-hole) term. Owing to the nature of the direct stochastic sampling of Σ_P , individual contributions to the polarization part cannot be simply disentangled. In the rest of the discussion, we thus distinguish only between exchange and (overall) polarization.

Exchange is in general larger, but we find many cases where the polarization is almost as big in magnitude. To analyze the size of the two terms, we fit the exchange-only contribution by a tight-binding-like expression:

$$\Delta(\Sigma_X) \simeq O_1 \Delta\left(\frac{1}{d_1}\right) + O_2 \Delta\left(\frac{1}{d_2}\right). \quad (4)$$

Here, O_1 and O_2 are fitted parameters, while d_1 and d_2 are the *average* interatomic distances and Δ refers to the change relative to the planar structure.

Due to the finite thickness of a single PNS, atoms on the “outside” and “inside” experience slightly different curvature and hence the interatomic distances vary. This is reflected in Eq. (4) by considering an average interatomic distance. Upon bending, the average distances increase as the dilatation of the outer-surface distances is larger than the compression of the inner surface ones, so $1/d$ decreases. For armchair bending both d_1 and d_2 change (the former about 10 times as much as the latter); for the zigzag bending only d_1 changes [51].

In our model [Eq. (4)], the bonding orbitals stabilize Σ_X : they have a negative value of $O_{1,2}$ and upon shortening of interatomic distances [i.e., when $\Delta(1/d_{1,2}) > 0$] the exchange self-energy becomes more negative [i.e., $\Delta(\Sigma_X) < 0$]. In contrast, the antibonding orbitals destabilize the QP energy as the atoms become closer, i.e., they are associated with positive values of $O_{1,2}$.

Table II contains the fitted $O_{1,2}$ coefficients for the HOMO, LUMO₁ and LUMO₂ (the latter for zigzag bending during which LUMO₂ has a p_x character). Note the reverse signs of O_1 and O_2 for HOMO and LUMO₁ (first two rows of Table II). The opposite signs indicate distinct bonding/antibonding characters along d_1 and d_2 for the two band-edge states. As mentioned in the previous paragraph, bending causes (on

TABLE III. Selected slopes (with respect to $1/R$) of the QP energies for several band-edge states; errors are estimated from the standard deviations of ε^{QP} from the linear fit. Slopes of the exchange self-energy are calculated from Eq. (4) using parameters from Table II.

	$\frac{\Delta\Sigma_X}{\Delta(1/R)}$ (eV nm)		$\frac{\Delta\varepsilon^{\text{QP}}}{\Delta(1/R)}$ (eV nm)	
	Zigzag	Armchair	Zigzag	Armchair
HOMO	-1.67	-1.24	-0.71 ± 0.02	-1.05 ± 0.05
LUMO ₁	2.07	1.20	1.05 ± 0.06	0.40 ± 0.10
LUMO ₂ (p_x)	-1.54		-2.91 ± 0.07	
LUMO ₂ (p_{x+z})				-0.66 ± 0.03

average) d_1 to increase much more than d_2 , i.e., the O_2 contribution results in smaller quantitative changes.

During bending along both directions, HOMO becomes less destabilized by the “antibonding interaction” along d_1 (O_1 term in Table II) and its energy decreases. In contrast, the energy of LUMO₁ increases since the “bonding interaction” (characterized by O_1) is getting smaller.

In bending along the armchair direction, this decrease/increase of the HOMO/LUMO₁ energy is counteracted by contributions from O_2 . However, zigzag bending does not affect d_2 , so $\Delta\Sigma_X$ shows much higher slopes for both HOMO and LUMO₁.

The overall change of the QP energy ($\Delta\varepsilon^{\text{QP}}$) with the curvature ($1/R$) is smaller than the change of Σ_X as shown in Table III and illustrated in Figs. 3 and 4. This is because of partial cancellation of $\Delta\Sigma_X$ by the changes in Σ_P , which in all cases studied raises the QP energy [52].

A similar consideration applies also to the LUMO₂ states which have distinct character for bending along the zigzag and armchair axes. In the first case, LUMO₂ has an overall antibonding p_x character [53], but we note that $\Delta\Sigma_X/\Delta(1/R)$ significantly underestimates the variation of ε^{QP} (by $\sim 50\%$ as shown in Table III and Figs. 3 and 4). The remaining part stems from the changes in the Hartree and external potential energies.

For bending along the armchair direction, LUMO₂ has a mixed p_z and p_x bonding character. Due to an increase of d_1 and d_2 with $1/R$, Σ_X increases (i.e., destabilizes LUMO₂) with a slope of 0.12 eV nm. This is similar to what happens with LUMO₁ (but the change is much smaller). This exchange effect is counterbalanced by large changes in Σ_P and the electrostatic potential. The LUMO₂ QP energy thus slightly decreases with energy.

Hence the behavior of the LUMO₂ states for bending along the zigzag and armchair axes has a different origin. While in the first case (zigzag bending), it is qualitatively given by variation of Σ_X , the response to bending in the armchair direction is governed by correlations and electrostatic effects. Combined, this leads to a very anisotropic response of the QP energies (and fundamental gaps) to bending.

V. CONCLUSIONS

Ab initio many-body perturbation theory was used here to study bending-induced changes of ε^{QP} and band gaps in PNS.

Extremely large PNSs containing 1958 valence electrons were studied for bending radii ranging between 1 μm and 2 nm along the armchair and zigzag directions. LDA-based DFT has a weaker response to bending than many-body perturbation theory, mostly due to the different response of the LUMO states to curvature.

Bending along the zigzag direction shows changes in the QP energies even for very small curvatures (which correspond to strains $\ll 1\%$) and a band gap decrease for $R > 100$ nm. This effect was not observed in the armchair direction (or is below the resolution of the stochastic method). Sample roughness leading to slight distortion would thus explain variation in experimental E_g as well as apparent in-gap states and peaks in scanning tunneling data [48].

Bending PNS to smaller radii $R < 100$ nm opens the fundamental band gap, regardless of the bending direction. Below $R \sim 4$ nm the unoccupied states reorder—for zigzag (but not for armchair) bending the gap starts closing. This effect is seen in both the DFT and many-body simulations, but is stronger by 50% in the latter. The gap changes depend on both the amount of bending and its direction. For the same material, we predict up to a 0.7 eV difference between the gaps at the same curvature but different bending directions.

We explained the emergence of the different response to bending by analyzing the individual energy contributions to the QP levels. The overall trends in the LUMOs stability were mostly due to the static exchange terms, which were dominated by the bonding or antibonding character of the nearest-neighbor orbital overlaps. However, dynamical screening dominates the changes in the gaps along the armchair direction. For large zigzag deformations, the first

unoccupied state has a p_x antibonding character. Its energy quickly decreases with further bending leading to a drop of E_g . For the same bending radii along the armchair direction, the first unoccupied state is a hybridized bonding combination of p_z and p_x . Due to competing exchange-correlation effects this hybridized state only weakly depends on curvature. Therefore, E_g keeps increasing with $1/R$ even for $R < 4$ nm for armchair bending.

Results for relaxed bent phosphorene nanosheets corroborate our prediction of LUMO reordering and strong E_g variation depending on the bending direction. Hence bending appears as a very efficient way to manipulate band gaps and orbital characters in phosphorene. Due to changes in the orbital shape and distribution, such modification could be very useful in understanding and developing optoelectronics and valleytronics devices [54].

ACKNOWLEDGMENTS

D.N. acknowledges support from NSF, Grant No. DMR-1611382. E.R. acknowledges support from the Department of Energy, Photonics at Thermodynamic Limits Energy Frontier Research Center, under Grant No. DE-SC0019140. R.B. acknowledges support from the US-Israel Binational Science foundation under the BSF-NSF program, Grant No. 2015687. The calculations were performed as part of the XSEDE [55] computational Project No. TG-CHE180051. The work also used resources of the National Energy Research Scientific Computing Center (NERSC), a U.S. Department of Energy Office of Science User Facility operated under Contract No. DE-AC02-05CH11231.

-
- [1] H. Liu, A. T. Neal, Z. Zhu, Z. Luo, X. Xu, D. Tománek, and P. D. Ye, *ACS Nano* **8**, 4033 (2014).
- [2] S. P. Koenig, R. A. Doganov, H. Schmidt, A. Castro Neto, and B. Özyilmaz, *Appl. Phys. Lett.* **104**, 103106 (2014).
- [3] L. Li, Y. Yu, G. J. Ye, Q. Ge, X. Ou, H. Wu, D. Feng, X. H. Chen, and Y. Zhang, *Nat. Nanotechnol.* **9**, 372 (2014).
- [4] V. Tran, R. Soklaski, Y. Liang, and L. Yang, *Phys. Rev. B* **89**, 235319 (2014).
- [5] D. Y. Qiu, F. H. da Jornada, and S. G. Louie, *Nano Lett.* **17**, 4706 (2017).
- [6] L. Li, J. Kim, C. Jin, G. J. Ye, D. Y. Qiu, H. Felipe, Z. Shi, L. Chen, Z. Zhang, F. Yang *et al.*, *Nat. Nanotechnol.* **12**, 21 (2017).
- [7] J. Kim, S. S. Baik, S. H. Ryu, Y. Sohn, S. Park, B.-G. Park, J. Denlinger, Y. Yi, H. J. Choi, and K. S. Kim, *Science* **349**, 723 (2015).
- [8] Q. Wei and X. Peng, *Appl. Phys. Lett.* **104**, 251915 (2014).
- [9] D. Akinwande, N. Petrone, and J. Hone, *Nat. Commun.* **5**, 5678 (2014).
- [10] F. Xia, H. Wang, and Y. Jia, *Nat. Commun.* **5**, 4458 (2014).
- [11] M. Buscema, D. J. Groenendijk, S. I. Blanter, G. A. Steele, H. S. Van Der Zant, and A. Castellanos-Gomez, *Nano Lett.* **14**, 3347 (2014).
- [12] W. Zhu, S. Park, M. N. Yogeesh, K. M. McNicholas, S. R. Bank, and D. Akinwande, *Nano Lett.* **16**, 2301 (2016).
- [13] F. Xia, H. Wang, D. Xiao, M. Dubey, and A. Ramasubramanian, *Nat. Photon.* **8**, 899 (2014).
- [14] F. Koppens, T. Mueller, P. Avouris, A. Ferrari, M. Vitiello, and M. Polini, *Nat. Nanotechnol.* **9**, 780 (2014).
- [15] L. Kou, T. Frauenheim, and C. Chen, *J. Phys. Chem. Lett.* **5**, 2675 (2014).
- [16] A. S. Rodin, A. Carvalho, and A. H. Castro Neto, *Phys. Rev. Lett.* **112**, 176801 (2014).
- [17] X. Peng, Q. Wei, and A. Copple, *Phys. Rev. B* **90**, 085402 (2014).
- [18] E. K. Gross and R. M. Dreizler, *Density Functional Theory* (Springer, Berlin, 1990), Vol. 337.
- [19] R. M. Martin, L. Reining, and D. M. Ceperley, *Interacting Electrons* (Cambridge University Press, Cambridge, UK, 2016).
- [20] L. Yu, A. Ruzsinszky, and J. P. Perdew, *Nano Lett.* **16**, 2444 (2016).
- [21] L. Hedin, *Phys. Rev.* **139**, A796 (1965).
- [22] F. Aryasetiawan and O. Gunnarsson, *Rep. Prog. Phys.* **61**, 237 (1998).
- [23] L. Hedin, *J. Phys.: Condens. Matter* **11**, R489 (1999).
- [24] J. Deslippe, G. Samsonidze, D. A. Strubbe, M. Jain, M. L. Cohen, and S. G. Louie, *Comput. Phys. Commun.* **183**, 1269 (2012).
- [25] M. Govoni and G. Galli, *J. Chem. Theory Comput.* **11**, 2680 (2015).

- [26] D. Neuhauser, Y. Gao, C. Arntsen, C. Karshenas, E. Rabani, and R. Baer, *Phys. Rev. Lett.* **113**, 076402 (2014).
- [27] V. Vlček, E. Rabani, D. Neuhauser, and R. Baer, *J. Chem. Theory Comput.* **13**, 4997 (2017).
- [28] V. Vlček, E. Rabani, and D. Neuhauser, *Phys. Rev. Mater.* **2**, 030801 (2018).
- [29] V. Vlček, W. Li, R. Baer, E. Rabani, and D. Neuhauser, *Phys. Rev. B* **98**, 075107 (2018).
- [30] D. Neuhauser, E. Rabani, and R. Baer, *J. Chem. Theory Comput.* **9**, 24 (2012).
- [31] R. Baer, D. Neuhauser, and E. Rabani, *Phys. Rev. Lett.* **111**, 106402 (2013).
- [32] D. Neuhauser, R. Baer, and E. Rabani, *J. Chem. Phys.* **141**, 041102 (2014).
- [33] E. Arnon, E. Rabani, D. Neuhauser, and R. Baer, *J. Chem. Phys.* **146**, 224111 (2017).
- [34] M. Chen, D. Neuhauser, R. Baer, and E. Rabani, *J. Chem. Phys.* **150**, 034106 (2019).
- [35] M. D. Fabian, B. Shpiro, E. Rabani, D. Neuhauser, and R. Baer, *WIREs Comput Mol Sci.*, e1412 (2019), doi: 10.1002/wcms.1412.
- [36] N. Levy, S. Burke, K. Meaker, M. Panlasigui, A. Zettl, F. Guinea, A. C. Neto, and M. Crommie, *Science* **329**, 544 (2010).
- [37] D.-M. Tang, D. G. Kvashnin, S. Najmaei, Y. Bando, K. Kimoto, P. Koskinen, P. M. Ajayan, B. I. Yakobson, P. B. Sorokin, J. Lou *et al.*, *Nat. Commun.* **5**, 3631 (2014).
- [38] M. S. Hybertsen and S. G. Louie, *Phys. Rev. B* **34**, 5390 (1986).
- [39] V. Vlček, R. Baer, E. Rabani, and D. Neuhauser, *J. Chem. Phys.* **149**, 174107 (2018).
- [40] L. Cartz, S. Srinivasa, R. Riedner, J. Jorgensen, and T. Worlton, *J. Chem. Phys.* **71**, 1718 (1979).
- [41] H. Xiao, X. Shi, F. Hao, X. Liao, Y. Zhang, and X. Chen, *J. Phys. Chem. A* **121**, 6135 (2017).
- [42] S. Plimpton, *J. Comput. Phys.* **117**, 1 (1995).
- [43] H. M. Aktulga, J. C. Fogarty, S. A. Pandit, and A. Y. Grama, *Parallel Comput.* **38**, 245 (2012).
- [44] G. J. Martyna and M. E. Tuckerman, *J. Chem. Phys.* **110**, 2810 (1999).
- [45] J. P. Perdew and Y. Wang, *Phys. Rev. B* **45**, 13244 (1992).
- [46] N. Troullier and J. L. Martins, *Phys. Rev. B* **43**, 1993 (1991).
- [47] Code is available at <http://www.stochasticgw.com/>.
- [48] L. Liang, J. Wang, W. Lin, B. G. Sumpter, V. Meunier, and M. Pan, *Nano Lett.* **14**, 6400 (2014).
- [49] F. A. Rasmussen, P. S. Schmidt, K. T. Winther, and K. S. Thygesen, *Phys. Rev. B* **94**, 155406 (2016).
- [50] S. I. Allec and B. M. Wong, *J. Phys. Chem. Lett.* **7**, 4340 (2016).
- [51] For the maximum bending, i.e., $R = 2$ nm, we achieve the largest change of the interatomic distance: on average d_1 is elongated by 9% for bending along both x and y axes, while d_2 changes merely by 1% and happens only for bending along the zigzag direction.
- [52] The change of Σ_p with curvature is 0.85/0.95 eV nm and $-0.84/-0.88$ eV nm for HOMO and LUMO₁ along the zigzag/armchair directions.
- [53] As mentioned in Sec. III B, the LUMO₂ state appears as antibonding only on the outer surface (with respect to the bending axis), while it is bonding on the inner surface. The former interaction dominates since the interatomic distances on the outer surface increase faster (≈ 3.5 faster) with $1/R$. Hence overall exchange contribution shows stabilization with decreasing bending radii; indeed Σ_x of p_x state decreases with slope of -1.37 eV nm.
- [54] J. R. Schaibley, H. Yu, G. Clark, P. Rivera, J. S. Ross, K. L. Seyler, W. Yao, and X. Xu, *Nat. Rev. Mater.* **1**, 16055 (2016).
- [55] J. Towns, T. Cockerill, M. Dahan, I. Foster, K. Gaither, A. Grimshaw, V. Hazlewood, S. Lathrop, D. Lifka, and G. D. Peterson, *Comput. Sci. Eng.* **16**, 62 (2014).